Available online at www.sciencedirect.com
SCIENCE DIRECT®
International Journal of Heat and Mass Transfer 47 (2004) 1573–1586
International Journal of HEAT and MASS TRANSFER
www.elsevier.com/locate/ijhmt

Comparisons of flow structure and local Nusselt numbers in channels with parallel- and crossed-rib turbulators

S.Y. Won, P.M. Ligrani *

Convective Heat Transfer Laboratory, Department of Mechanical Engineering, University of Utah, MEB 2110, 50 S. Central Campus Drive, Salt Lake City, UT 84112-9208, USA

Received 30 July 2003; received in revised form 31 October 2003

Abstract

Spatially-resolved-local flow structure, spatially-averaged flow structure, and surface Nusselt numbers are presented and compared for stationary channels with aspect ratios of 4 and rib turbulators inclined at 45°. Two different rib arrangements with perpendicular and parallel orientations on two opposite surfaces are investigated at Reynolds numbers (based on channel height), Re_H from 480 to 18,300. Comparisons show important local Nusselt number differences for the two rib arrangements, especially just upstream of the ribs, which are due to significant differences in global and local primary- and secondary-flow characteristics.

1. Introduction

Rib turbulators are one of several techniques which are used for enhancing convective heat transfer rates by increasing secondary advection, and three-dimensional turbulence transport over large portions of flow fields. The present study is conducted using channels with aspect ratio of 4, with ribs oriented at 45° with respect to the streamwise flow direction, and placed both perpendicular and parallel to each other on opposite sides of the two widest walls. These single-passage channels model internal cooling passages employed near the mid-chord and trailing edge regions of turbine airfoils used in gas turbine engines for utility power generation. Spatially-resolved flow structure (instantaneous and time-averaged), and surface Nusselt numbers and friction factors are respectively measured and compared for both crossed- and parallel-rib turbulators. These flow field structural characteristics are obtained because they aid the development of numerical models and prediction schemes, and because they provide important insight into the flow phenomena responsible for local heat transfer coefficient augmentations. However, in spite of the value of flow structure data, obtained together with heat transfer data, very few papers present such data together for channels with rib turbulators.

Existing papers in this area discuss a variety of arrangements, including single-pass and multi-pass channels, square and rectangular channels, channels with and without rotation, and rotating channels with different orientations with respect to the axis of rotation [1–16]. Like the present investigation, several of the earliest ribbed channel studies consider single pass, stationary channels with no rotation. Of these studies, Han et al. [1] address the effects of rib shape, angle of attack, and pitch-to-height ratio. According to these investigators, ribs with 45° inclinations produce better heat transfer performance than ribs with 90° orientations, when compared at the same friction power. Han and Park [2] vary the channel aspect ratio, and conclude that the best heat transfer performance is obtained using a square channel with a rib turbulator angle of attack from 30° to 45°. Han et al. [3] indicate that best heat transfer enhancements in square channels are produced by V-shaped ribs with 45° and 60° arrangements, followed by 45° and 60° parallel ribs, which are followed by 45° and 60° crossed ribs. Han et al. [4] investigate wedge-shaped and delta-shaped turbulence promoters in square channels, and compare their performance with existing

* Corresponding author. Tel.: +1-801-581-4240; fax: +1-801-585-9826.
E-mail address: ligrani@mech.utah.edu (P.M. Ligrani).

0017-9310/$ - see front matter © 2003 Elsevier Ltd. All rights reserved.
doi:10.1016/j.ijheatmasstransfer.2003.10.026

Nomenclature

a	streamwise extent of test surface
b	spanwise extent of test surface
D_h	channel hydraulic diameter
e	rib turbulator width
e'	rib turbulator width in streamwise direction
H	channel height
h	heat transfer coefficient based on flat projected area, $\dot{q}_0''/(T_w - T_m)$
k	thermal conductivity
Nu	local Nusselt number, hD_h/k
Nu_0	baseline Nusselt number in a smooth channel with no rib turbulators
p	streamwise pitch spacing of rib turbulators
P	time-averaged local static pressure
Pr	Prandtl number
$\dot{q}_0''$	surface heat flux
Re_H	Reynolds number based on channel height, $\overline{V}H/v$
Re_{D_h}	Reynolds number based on hydraulic diameter, $\overline{V}D_h/v$
T	local static temperature
u_x	time-averaged local streamwise component of velocity
u_y	time-averaged local normal component of velocity
u_z	time-averaged local spanwise component of velocity
$\overline{V}$	time- and spatially-averaged velocity across the channel cross-section
X	streamwise coordinate measured from the test section inlet
Y	normal coordinate measured from the test surface between the ribs
Z	spanwise coordinate measured from the test surface centerline

Greek symbols

ρ_a	air density at test section inlet
ω_x	time-averaged local streamwise vorticity
v	kinematic viscosity

Subscripts

a	ambient value
i	test section inlet value
m	time-averaged, local mixed-mean value
o	total or stagnation value
w	local wall value

data for different types of rib turbulators. Delta-shaped ribs generally perform better than the wedge-shaped ribs, especially when the delta-shaped ribs on opposite walls are aligned, and arranged with a backward flow direction. Taslim et al. [5] provide additional evidence that 45° ribs produce higher thermal performance factors than 90° ribs. The authors also indicate that, of the configurations examined, the highest heat transfer enhancements and highest friction factors are produced by low-blockage ratio V-shaped ribs. In a later study, Taslim et al. [6] study 12 different geometries of ribs that are placed on all four walls of channels with both square and trapezoidal cross sections. Compared to channels with ribs on two walls, heat transfer coefficients and thermal performance factors are enhanced. More recently, Casarsa et al. [7] characterize the velocity and heat transfer fields in an internal cooling channel with 90° ribs which produce 30 percent blockage. Included are heat transfer enhancement magnitudes, time-averaged distributions of mean velocity components, and time-averaged distributions of normalized root-mean-square velocity fluctuations. Ligrani and Mahmood [8] present spatially-resolved Nusselt numbers and flow structure are for a stationary channel with an aspect ratio of 4 and angled rib turbulators inclined at 45° with perpendicular orientations on two opposite surfaces. The ratio of rib height to hydraulic diameter is 0.078, the rib pitch-to-height ratio is 10, and the blockage provided by the ribs is 25 percent of the channel cross-sectional area. According to these authors, spatially-resolved local Nusselt numbers are highest on tops of the rib turbulators, with lower magnitudes on flat surfaces between the ribs, where regions of flow separation and shear layer re-attachment have pronounced influences on local surface heat transfer behavior. Also important are intense, highly unsteady secondary flows and vortex pairs, which increase secondary advection and turbulent transport over the entire channel cross-section.

Wang et al. [9] present heat transfer results from square ducts with 45° ribs. Thurman and Poinsatte [10] measure heat transfer and bulk air temperature in a three-pass duct with orthogonal ribs and bleed holes both located on one wall. According to these investigators, changing the locations of the ribs relative to the holes produces large changes to surface heat transfer coefficient distributions. Cho et al. [11] employ continuous and discrete, parallel and cross arrays of ribs in a single-pass square duct. Discrete ribs with gaps in between are found to produce more uniform heat transfer coefficient distributions than continuous ribs. Using experimental and numerical approaches, Bonhoff et al. [12] investigate the flow characteristics within coolant channels with 45° ribs. They predict the complex flow features, namely the re-circulation zones and vortices

behind the ribs, and the secondary motion through the channel with three different turbulence models. Schabacker et al. [13] examine three-dimensional flow development in the straight and curved portions of a passage with ribs. Oblique ribs in the straight portions contribute to the development of secondary flows that transport fluid from the central parts of the channel towards the walls. Acharya et al. [14] describe the generation of secondary flows in rotating two-pass coolant channels using several different types of profiled ribs. According to these authors, the profiled ribs generally enhance heat transfer over the baseline arrangement by generating secondary flows and longitudinal vorticity that interact with the Coriolis induced secondary flows.

The present experimental study is conducted using a large-scale test section, without rotation, so that detailed, spatially-resolved flow structural characteristics and surface Nusslet numbers can be measured. Reynolds numbers, based on channel height, range from 480 to 18,300. The results are new and unique because local instantaneous flow structure, local time-averaged flow structure, time-spatially-averaged flow structure, and local surface Nusselt numbers are compared for the crossed- and parallel-rib arrangements. The resulting pictures, illuminated by these data, are of complex, three-dimensional, time-varying flow fields with significant flow losses and heat transfer augmentations.

2. Experimental apparatus and procedures

The overall experimental apparatus is similar to the ones described by Ligrani and Mahmood [8], and Mahmood et al. [15,16]. A brief description of this apparatus is also presented here.

2.1. Channel for flow structure measurements

A schematic diagram of the facility used for flow visualizations and flow structural measurements is shown in Fig. 1a. This facility is an open-loop, suction flow type of device. At the inlet of the facility, the air passes from the laboratory into a rectangular bell mouth inlet, followed by a honeycomb, two screens, and a two-dimensional nozzle with a contraction ratio of 5.6. This nozzles leads to a boundary layer bleed on the top and bottom walls followed by a rectangular cross-section, 411 mm by 103 mm inlet duct which is 1219 mm in length, with an aspect ratio of 4. This is equivalent to 7.4 hydraulic diameters (where hydraulic diameter is 164.7 mm). Two trips are employed on the top and bottom surfaces of the inlet duct. Each of these is about 3 mm high, and extends across the span of the channel width, just upstream of the test section, which follows with the same cross-section dimensions and aspect ratio. The test section exits to a 0.60 m square plenum, which is followed by two pipes, each containing an orifice plate. The pressure drop across one or the other of these orifice plates (measured using a Validyne M10 digital pressure manometer) is used to determine the air mass flow rate, using standard ASME procedures. The pipe then exits into a second larger plenum, containing an ILG Industries type 10P centrifugal blower and a Dayton 2C864 centrifugal blower, which are employed to induce flow through the test section. From this second plenum, the air in the facility then exits to a vent, and then to the atmosphere.

2.2. Test surface geometry details

Fig. 1c and d give the geometric details of the test surfaces, including crossed- and parallel-rib turbulator geometries. A total of 13 acrylic ribs or rib segments are used on the top wall and on the bottom wall of each test section. As mentioned, these are arranged with 45° angles with respect to the streamwise flow direction, such that the ribs on opposite walls of the channel are either perpendicular or parallel to each other. The ribs are arranged as shown in Fig. 1c and d, such that the ribbed test section is appended to the end of the smooth inlet duct. Each rib has 12.8 mm height and square cross-section. The ratio of rib height to hydraulic diameter is 0.078, the rib pitch-to-height ratio is 10, and the blockage provided by the ribs is 25 percent of the channel cross-sectional area. The top wall of the test section also has two cut-out regions (one at the upstream end and one at the downstream end) where a zinc–selenide window can be installed to allow the infrared camera to view a portion of the test surface on the bottom wall. When this window is not in use, inserts with ribs (which exactly match the adjacent rib turbulators on the top wall) are used in its place. To avoid the presence of unwanted flow disturbances, this ribbed insert is employed as all flow characteristics are measured in the channel. Also identified in Fig. 1c and d is the test section coordinate system employed for the study. Note that the Y coordinate is directed normal to the bottom wall.

2.3. Time-averaged flow velocity components and pressure

A 1.27 mm diameter miniature five-hole pressure probe, manufactured at the University of Utah especially for these measurements, is used to obtain time-averaged surveys of total pressure, static pressure, and the three mean velocity components. These data are then used to deduce distributions of streamwise vorticity. To obtain the surveys, the probe employed is mounted on an automated two-dimensional traverse, and inserted into the test section through a slot lined with foam to prevent air leakage. The centerline of this probe is traversed as close as about 5 mm from the

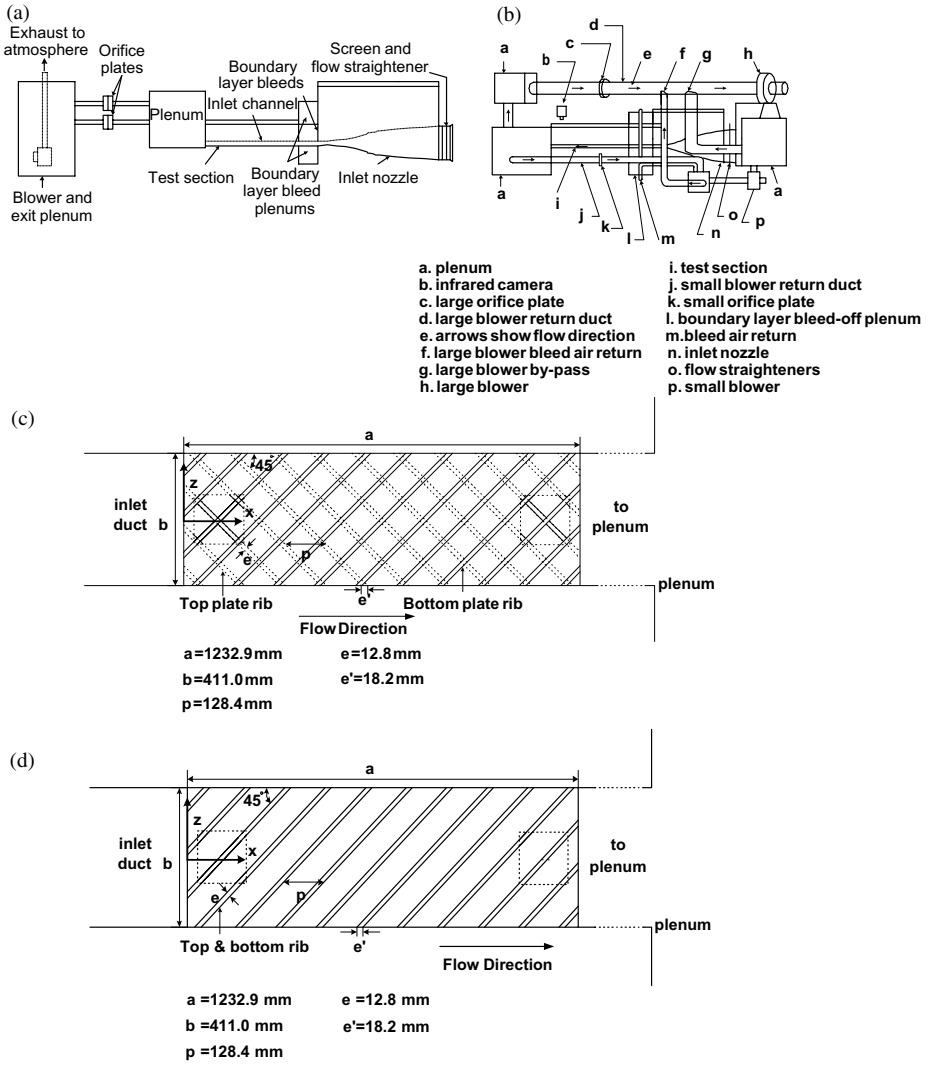

Fig. 1. Schematic diagrams of: (a) the experimental apparatus used for flow visualizations and measurements of flow structure, (b) the experimental apparatus used for heat transfer measurements, (c) the crossed-rib turbulator test surfaces, including coordinate system, (d) the parallel-rib turbulator test surfaces, including coordinate system.

test section top wall, and as close as approximately 5 mm from the test section bottom wall. The output ports of the probe are connected either to Validyne DP103-06 pressure transducers (to measure differential pressures up to 2.5 mm of water), or Celesco LCVR pressure transducers (to measure differential pressures up to 20.0 mm of water). Signals from the transducers are then processed using Celesco CD10D Carrier-Demodulators. Voltages from the Carrier-Demodulators are acquired using a Hewlett-Packard 44422A data acquisition card installed in a Hewlett-Packard 3497A data acquisition control unit. This control unit, two Superior Electric type M092-FD310 Mitas stepping motors on the two-dimensional traverse, a Superior Electric Modulynx Mitas type PMS085-C2AR controller, and a Superior Electric Modulynx Mitas type PMS085-D050 motor drive are controlled by a Hewlett-Packard A4190A Series computer. Contour plots of measured quantities are generated using a polynomial interpolating technique (with DeltaGraph software) between data points. In each survey plane, 1560 data points are spaced 2.54 mm apart. Data obtained at each one of these locations is time-averaged over a period of about 30 s. Additional details of the five-hole probe measurement procedures, including calibration details and procedures to account for velocity gradients and finite spatial resolution, are given by Ligrani et al. [17,18].

2.4. Flow visualization

Flow visualization using smoke is used to identify vortex structures and other secondary flow features. Smoke from three and four horizontally-oriented smoke wires is employed for this purpose. These are located 4.8, 11.9, 88.5, and 95.7 mm from the bottom test surface at $X = 1258$–1261 mm for crossed-rib turbulators, and are located 20, 50, and 80 mm from the bottom test surface at $X = 209$ mm for parallel-rib turbulators. To produce sheets of smoke, each wire is first coated with Barts Pneumatics Corp. super smoke fluid and then powered using a Hewlett-Packard 6433B DC power supply. With this arrangement, the smoke forms into single thin planes parallel to the test surface. As the smoke is advected downstream, the secondary flows which accompany vortex and secondary flow development cause the smoke to be re-arranged in patterns which show the locations and distributions of these flow phenomena. Smoke patterns are illuminated in spanwise-normal light planes located at $X = 1462$ mm for the crossed-rib channel, and at $X = 620$ mm for the parallel-rib channel using a thin sheet of light provided by a Colotran ellipsoidal No. 550, 1000 W spot light, and a slits machined in two parallel metal plates. Images are recorded using a Panasonic WV-BP330 CCTV video camera, connected to a Panasonic AG-1960 type 4-head, multiplex video cassette recorder. Images recorded on video tape (taken individually or in sequence) are then digitized using a Scion Image Corporation Frame grabber video card, and Scion image v.1.9.2 software. The resulting images are then further processed using a Dell P4 Precision 330 PC computer. Additional discussion of many of the procedures used for flow visualization is provided by Ligrani [19].

2.5. Channel for heat transfer measurements

A separate channel facility (but with the same test section), and the same interior geometry identical to that in the flow structure facility, is employed for heat transfer measurements. A schematic drawing of this facility is shown in Fig. 1b. The air used within the facility is circulated in a closed-loop. In each case, the air mass flow rate from the test section is measured (upstream of which ever blower is employed) using an ASME standard orifice plate and Validyne M10 digital pressure manometer. The blower then exits into a series of two plenums (0.9 m square and 0.75 m square). A Bonneville cross-flow heat exchanger is located between two of these plenums, and is cooled with liquid nitrogen at flow rate appropriate to give the desired air temperature at the exit of the heat exchanger. As the air exits the heat exchanger, it enters the second plenum, from which the air passes through the same types of flow management devices employed in the channel used for the flow structural measurements. These are followed by a 1219 mm long inlet duct, and the same test section used for the flow structural measurements.

All exterior surfaces of the facility (between the heat exchanger and test section) are insulated with Styrofoam ($k = 0.024$ W/m K), or 2–3 layers of 2.54 cm thick, Elastomer Products black neoprene foam insulation ($k = 0.038$ W/m K) to minimize heat losses. Calibrated copper–constantan thermocouples are located between the three layers of insulation located all around the test section to determine conduction losses. Between the first layer and the 3.2 mm thick acrylic test surfaces are custom-made Electrofilm etched-foil heaters (each encapsulated between two thin layers of Kapton) to provide a constant heat flux boundary condition on the inner faces of all four of the test surfaces employed in the test section. Surface heat flux rates of about 370 W/m^2 for crossed-rib turbulators and 420 W/m^2 for parallel-rib turbulators are employed for Re_H of 18,300 and 17,000, respectively. The acrylic surfaces, which are adjacent to the airstream, contain 35 copper–constantan thermocouples, which are placed within the ribs as well as within the flat portions of the test surface between the ribs. Each of these thermocouples is located 0.051 cm just below this surface to provide measurements of local surface temperatures, after correction for thermal contact resistance and temperature drop through the 0.051 cm thickness of acrylic. Acrylic is chosen because of its low thermal conductivity ($k = 0.19$ W/m K at 20 °C [20]) to minimize streamwise and spanwise conduction along the test surface, and thus, minimize ''smearing'' of spatially varying temperature gradients along the test surface. The power to the foil heater is controlled and regulated using a variac power supply. Energy balances, performed on the heated test surface, then allow determination of local magnitudes of the convective heat flux. These flux levels are based upon flat test surface areas.

The mixed-mean stagnation temperature of the air entering the test section is measured using five calibrated copper–constantan thermocouples spread across its cross-section. To determine this temperature, thermocouple-measured temperatures are corrected for thermocouple wire conduction losses, channel velocity variations, as well as for the differences between stagnation and recovery temperature. Magnitudes of mixed-mean temperature along the test surface are then determined using energy balances along with the measured mixed-mean temperature at the test section inlet. All measurements are obtained when the test facility is steady-state.

2.6. Local Nusselt number measurement

To determine the surface heat flux (used to calculate heat transfer coefficients and local Nusselt numbers), the convective power levels provided by the

etched foil heaters are divided by flat test surface areas. Spatially-resolved Nusselt number distributions along the bottom-rib turbulator test surface are determined using infrared imaging in conjunction with thermocouples, energy balances, and in situ calibration procedures. To accomplish this, the infrared radiation emitted by the heated interior surface of the channel is captured using a VideoTherm 340 Infrared Imaging Camera, which operates at infrared wave lengths from 8 to 14 μm. Temperatures, measured using the calibrated, copper–constantan thermocouples distributed along the test surface adjacent to the flow, are used to perform the in situ calibrations simultaneously as the radiation contours from surface temperature variations are recorded. This is accomplished as the camera views the test surface through a custom-made, zinc–selenide window (which transmits infrared wave lengths between 6 and 17 μm) located on the top wall of the test section. The window is located just above portions of the 10th, 11th, and 12th ribs downstream from the leading edge of the test surface. The exact spatial locations and pixel locations of these thermocouple junctions and the coordinates of a 12.7 cm by 12.7 cm field of view are known from calibration maps obtained prior to measurements. During this procedure, the camera is focused, and rigidly mounted and oriented relative to the test surface in the same way as when radiation contours are recorded.

Images from the infrared camera are recorded as 8-bit gray scales directly into the memory of a Dell Dimension XPS T800r PC computer using a Scion Image Corporation Frame grabber video card, and Scion image v.1.9.2 software. Three sets of 60 frames are recorded at a rate of one frame per second. This is done after the rib turbulator flows are established to obtain data when the test surface is at a steady-state condition. All of 180 resulting images are then ensemble-averaged to obtain the final gray scale data image. This final data set is then imported into Matlab version 6.0.0.88 (Release 12) software to convert each of 256 possible gray scale values to local Nusselt number values, at each pixel location using calibration data. Each resulting individual image then covers a 300 pixel by 300 pixel area. Thermal conductivity in the Nusselt number is based on the average of the local wall temperature and the temperature of the air at the upstream inlet. Sargent et al. [21], Ligrani and Mahmood [8], and Mahmood et al. [15,16] provide additional details on portions of the infrared imaging and measurement procedures.

2.7. Conduction analysis with the test surface

Three-dimensional conduction along and within the test surface is determined using version 6.0 of the ANSYS numerical code. To accomplish this, a portion of the test surface, with one rib segment, is modeled using approximately 17,480 numeric node elements. In addition, a constant heat flux boundary condition (determined from values used in the experiments) is imposed on the back side of the 3.2 mm thick acrylic test surface. Local surface temperatures, measured experimentally using infrared thermography, are used for the thermal boundary condition on portions of the test surface next to the air stream, including the top of the rib segment and the flat parts of the test surface around the rib. Temperatures are also imposed as the thermal boundary condition on the vertical parts of the rib segment, which are determined by interpolation of values measured at the edge of the rib top and at the corner (between each rib side and flat parts of the test surface) [8].

Ordinarily, without the conduction analysis applied, the same heat flux produced by the etched-foil heater is assumed to leave the test surface next to the air stream at the rib top and along the flat parts of the test surface around the rib. This means that no heat is assumed to leave the vertical side walls of the rib, and that all of the thermal power into the test surface leaves entirely only from the horizontal surfaces next to the air stream. The ANSYS version 6.0 conduction analysis is used to determine the non-uniform variations of surface heat flux into the air stream, which are actually present, including along the vertical sides of the rib segment. As mentioned, this is accomplished using experimentally measured values as thermal boundary conditions around the numerical domain solved by the numerical code [8].

2.8. Uncertainty estimates

Uncertainty estimates are based on 95 percent confidence levels, and determined using procedures described by Kline and McClintock [22] and Moffat [23]. The experimental uncertainties of time-averaged magnitudes of local total pressure (relative to atmospheric pressure), local static pressure (relative to atmospheric pressure), local streamwise velocity, and local streamwise vorticity are ±4.0, ±4.0, ±2.5, and ±8.0 percent, respectively. The estimated uncertainty of the time-averaged magnitude of the spanwise velocity component is about ±4.0 percent. Uncertainty of temperatures measured with thermocouples is about 0.2 °C. Spatial and temperature resolutions achieved with the infrared imaging are about 0.52 mm and 0.8 °C, respectively. This magnitude of temperature resolution is due to uncertainty in determining the exact locations of thermocouples with respect to pixel values used for the in situ calibrations. Local Nusselt number ratio uncertainty is then about ±0.13 (for a ratio of 2.00), or about ±6.5 percent. Reynolds number uncertainty is approximately ±1.7 percent for Re_H of 10,000.

3. Experimental results and discussion

3.1. Local instantaneous flow structure

Fig. 2a and b compare instantaneous flow visualization images obtained at different Reynolds numbers from the channels with crossed-ribs and the parallel ribs. These data, as wall as the sketches in Fig. 2c and d, are given to illustrate overall flow behavior in the channels which result from the two different rib arrangements. The data are obtained at relatively low Reynolds numbers from 480 to 1400 because diffusion and increased unsteadiness at higher Reynolds numbers result in smeared and unrecognizable flow patterns. Each image in Fig. 2a and b extends in the vertical direction from the bottom to the top of the channel, and in the horizontal direction over a distance of about 1.5 channel heights for the crossed-rib channel, and 3.0 channel heights for the parallel-rib channel. The images are illuminated in spanwise-normal planes located at $X = 1462$ mm in the channel with the crossed ribs, and at $X = 620$ mm in the channel with the parallel ribs. The coordinate systems for the images are also included in the figures.

The overall secondary flow patterns produced by the crossed- and parallel-rib arrangements are shown in Fig. 2c and d, respectively. When viewed in flow cross-sectional planes, the channel with the crossed-ribs produces one single, large cell of fluid motion. Two cells of large scale fluid motion are present with the parallel-rib arrangement, such that one is located in the top half of the channel and one is located in the bottom half of the channel. With the same rib angles with respect to the streamwise flow direction, the magnitudes of secondary flows near the surface are expected to have roughly the same magnitudes near the walls.

Evidence of these large-scale secondary flows are apparent in Fig. 2a and b. For the crossed ribs, this is indicated by vortex pairs that are highly skewed, such that one vortex in each pair is larger than the other. For the parallel ribs, the large-scale secondary flows are indicated by pathlines of smoke moving in the negative Z/H direction in the central part of the channel, and in the positive Z/H direction near the top and bottom walls. The flow visualization images in Fig. 2a and b also show evidence of a variety of other smaller-sized secondary flows, with length scales ranging from spanwise

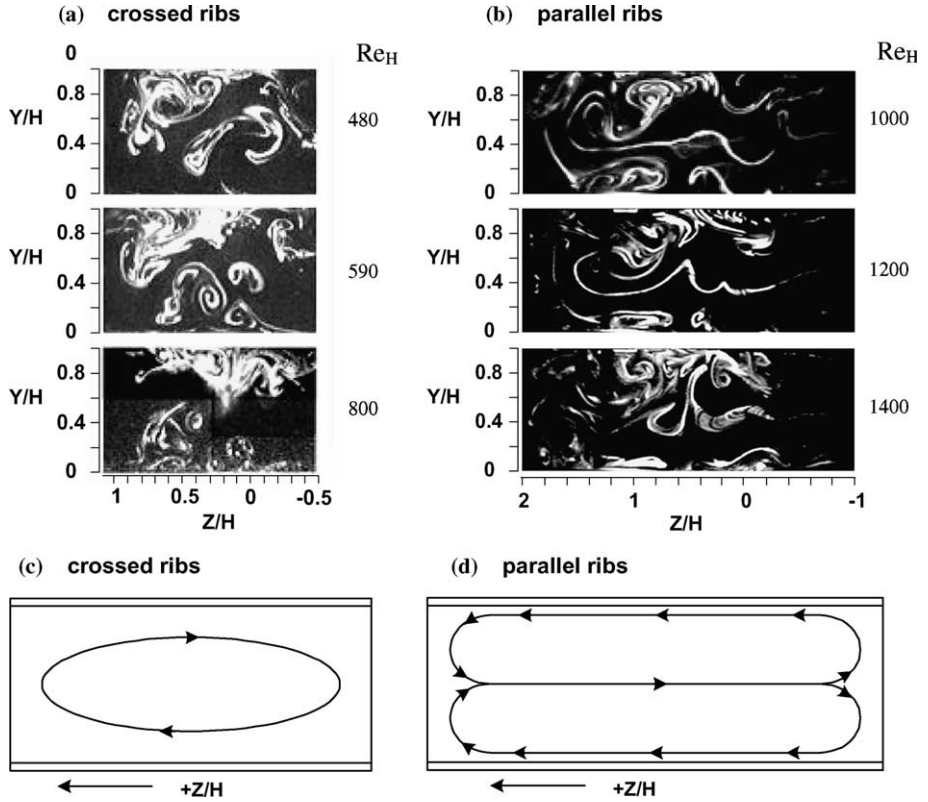

Fig. 2. Instantaneous flow visualization images illuminated in a spanwise-normal plane, including coordinate system locations, for different Reynolds numbers. (a) $X = 1462$ mm for crossed-rib turbulators. (b) $X = 620$ mm for parallel-rib turbulators. (c) Overall secondary flow structure in cross-sectional plane of channel with crossed ribs. (d) Overall secondary flow structure in cross-sectional plane of channel with parallel ribs.

rib spacing to very small. These are partially induced by local flow interactions with the ribs, and are in the form of single vortices, vortex pairs, as well as other swirls and whirls of fluid motion. These are partially induced by viscous effects, continuity, and the influences of the ribs, as they force air to and from the top and bottom test surfaces. The crossed- and parallel-rib data in Fig. 2a and b provides some indication that larger-sized vortex pairs are sometimes replaced by collections of multiple, smaller vortex pairs as the Reynolds number increases. The data in Fig. 2a and b are obtained when the flow in the ribbed channel is mostly laminar. At higher Re_H, when the flow in the ribbed channel is fully turbulent, a similar variety of different flow structures are likely to be present, existing over a wide range of length scales. Regardless of whether crossed or parallel ribs are employed, such structures, the vortices and secondary flows which accompany them, aid convective processes for turbulent heat transfer augmentation by: (i) increasing secondary advection of fluid between the central parts of the channel and regions near the wall, and (ii) producing regions with high, three-dimensional shear and high magnitudes of turbulence production over much of the channel cross section, thereby substantially increasing turbulence transport levels in all three coordinate directions.

3.2. Local time-averaged flow structure

Time-averaged data also provide evidence of substantial secondary flows, significant mixing, and significant losses in the rib turbulated channels. These data are presented in Figs. 3–6, and are measured at Re_H of 6000, 8000, 10,000, and 15,000 and $X = 1235$ mm, which is located just downstream of the test sections for both the parallel and crossed-ribbed channels. The surveys which are presented in Fig. 3, are made for $Re_H = 15,000$ over a spanwise-normal plane in the channel with the parallel ribs. Each survey extends about one channel height in the vertical direction, and about three channel heights in the horizontal direction. Given in Fig. 3a–e are normalized distributions of streamwise velocity, total pressure, static pressure, spanwise velocity, and streamwise vorticity, respectively. The locations of the downstream ends of four of the ribs (two on the top surface and two on the bottom surface) are indicated within each survey in Fig. 3.

The survey of normalized streamwise vorticity in Fig. 3e generally shows that positive vorticity is generally present over the top part of the channel, and that negative vorticity is generally present over the bottom part of the channel. This is consistent with the overall flow behavior shown in Fig. 2d. The strong, spanwise secondary flows induce other smaller-scale, secondary flows in the channel with the parallel-rib turbulators, as mentioned. Evidence of these is provided by regions of

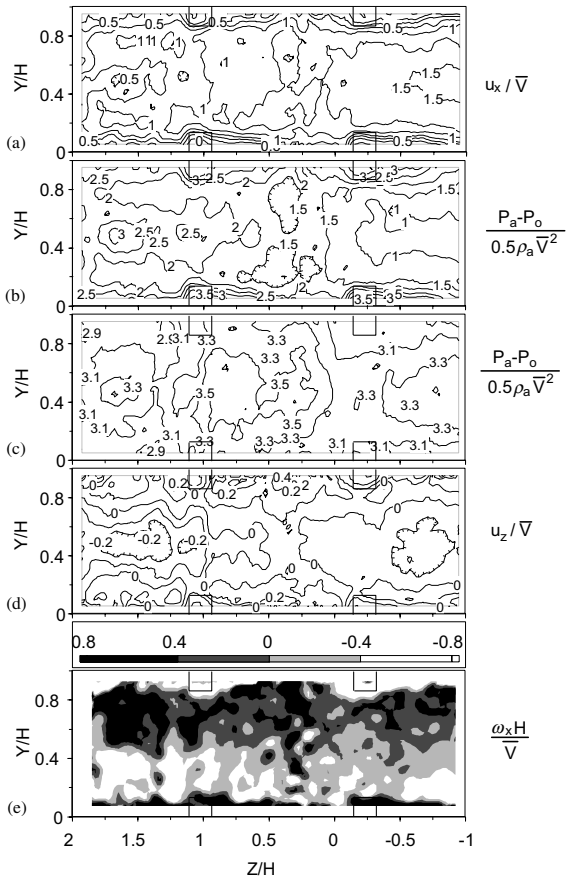

Fig. 3. From surveys conducted in a spanwise-normal plane at $X = 1235$ mm for $Re_H = 15,000$ for parallel-rib turbulators, normalized, time-averaged surveys of: (a) local streamwise velocity, (b) local total pressure, (c) local static pressure, (e) local spanwise component of velocity, and (e) local streamwise vorticity.

positive and negative normalized streamwise vorticity, which are adjacent to each other, in the time-averaged streamwise vorticity survey shown in Fig. 3e. This includes numerous local positive regions near the top wall and several local negative regions near the bottom wall. These are qualitatively consistent with the flow visualization images in Fig. 2b, since visualized vortex pairs in this figure are located at roughly the same positions as local fluid swirls and/or regions of higher streamwise vorticity in Fig. 3e.

The distribution of the normalized and time-averaged spanwise velocity component u_z in Fig. 3d is also consistent with the large-scale-secondary flows produced by the parallel ribs which are shown in Fig. 2d. Here, the spanwise secondary flows are generally moving in the $+Z/H$ direction near the top and bottom walls, and in the negative Z/H direction near the central part of the channel. Such motions are of course tied to continuity

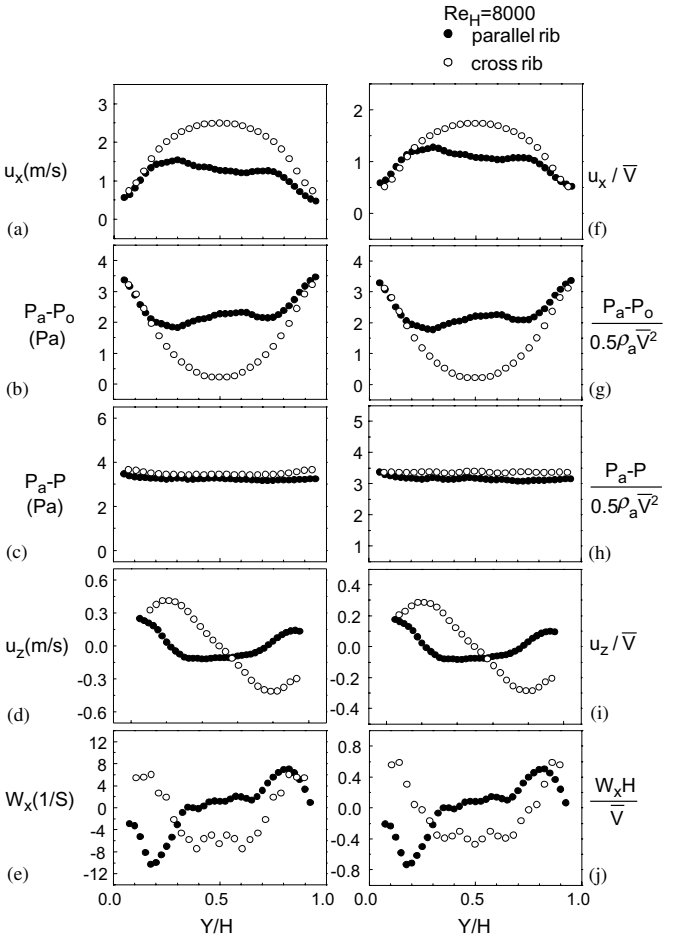

Fig. 4. From surveys conducted in a spanwise-normal plane at $X = 1235$ mm for $Re_H = 8000$ with crossed- and parallel-rib turbulators, comparisons of spanwise-averaged and time-averaged profiles of: (a) local streamwise velocity, (b) local total pressure, (c) local static pressure, (d) local spanwise component of velocity, (e) local streamwise vorticity, (f) normalized local streamwise velocity, (g) normalized local total pressure, (h) normalized local static pressure, (i) normalized local spanwise component of velocity, and (j) normalized local streamwise vorticity.

considerations, and largely induced by the inclinations of the ribs with respect to the $+X$ direction, as well as the same rib orientations on the top and bottom surfaces of the channel.

Such secondary fluid motions also influence the distributions of streamwise velocity, stagnation pressure, and static pressure in Fig. 3a–c. Distributions of normalized time-averaged streamwise velocity and total pressure deficits are consistent with each other, with generally higher magnitudes in the central part of the channel. Lower streamwise velocity magnitudes and higher total pressure deficits are then present near the top and bottom walls. In both cases, velocity magnitudes, and pressure deficits in the central part of the channel decrease as Z/H increase and the channel endwall is approached at $Z/H = 2$. Signatures due to flow separations and re-circulation zones are also apparent near individual-rib locations in Fig. 3a and b. Note that $\overline{V}$, the time-averaged velocity which is spatially-averaged over the channel cross-section, is used to normalize the data in Fig. 3, as well as the data which are presented in subsequent figures. This is the same velocity which is used to deduce the Reynolds number Re_H. It is generally slightly lower than values deduced from averaging locally-measured u_x values because local values are not measured in immediate vicinity of the ribbed walls, where values are lowest.

The static pressure distribution in Fig. 3c is qualitatively different from the velocity and stagnation pressure distributions in Fig. 3a and b. Larger static pressure deficits are generally present near the central parts of the channel. Other, additional local variations are also evident, which are mostly due to some local curvature of streamlines in the time-averaged flow field.

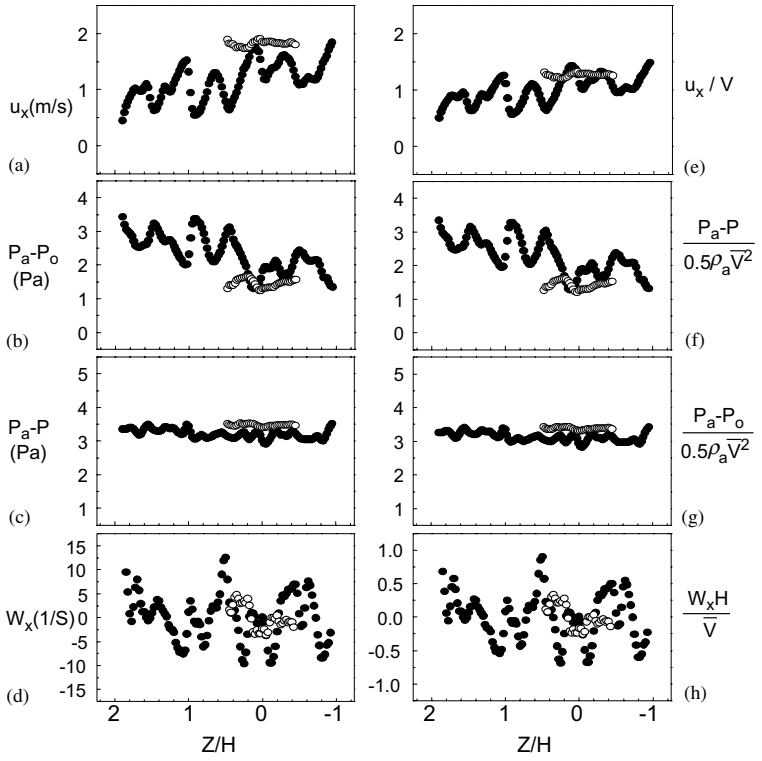

Fig. 5. From surveys conducted in a spanwise-normal plane at $X = 1235$ mm for $Re_H = 8000$ with crossed- and parallel-rib turbulators, comparisons of normal-averaged and time-averaged profiles of: (a) local streamwise velocity, (b) local total pressure, (c) local static pressure, (d) local streamwise vorticity, (e) normalized local streamwise velocity, (f) normalized local total pressure, (g) normalized local static pressure, and (h) normalized local streamwise vorticity. Symbols are defined in Fig. 4.

Fig. 4a–j compare *spanwise-averaged* profiles of normalized streamwise velocity, total pressure, static pressure, spanwise velocity, and streamwise vorticity as they vary with Y/H for $Re_H = 8000$ for both the crossed- and parallel-rib arrangements. Dimensional magnitudes are given in parts a–e, and non-dimensional magnitudes are presented in parts f–j of this figure. Each data point in each profile is obtained by averaging survey data in the Z/H direction as Y/H is held constant. Variations here are again tied to overall secondary flow structure shown in Fig. 2c and d. For example, the spanwise velocity component in Fig. 4d and i is positive and moves in the $+Z/H$ direction, near both channel walls, when parallel ribs are present. In contrast, span- and time-averaged spanwise velocity motion is in the positive or $+Z/H$ direction in the bottom half of the channel only (i.e. for $Z/H < 0.5$) with crossed ribs, with negative magnitudes when $Z/H > 0.5$. Note that absolute value magnitudes of spanwise velocity are roughly the same at the measurement station nearest to the wall for both spanwise-averaged-rib arrangements. Spanwise-averaged streamwise vorticity magnitudes for the parallel and crossed ribs in Fig. 4e and j are also similar in absolute value magnitude near the top and bottom walls ($Y/H < 0.15$, $Y/H > 0.85$), but with opposite signs near the bottom wall at $Y/H = 0$, and similar signs near the top wall at $Y/H = 1.0$. The overall secondary flows shown in Fig. 2c and d lead to pressure losses which are greater for the parallel ribs than for crossed ribs. This is because the two secondary flow cells produced by the parallel ribs are move efficient (than the single cell structure produced by the crossed ribs) in advecting fluid with low streamwise momentum and larger stagnation pressure deficits to the central parts of the channel. Overall total pressure losses are also larger, and streamwise velocity magnitudes in the central part of the channel are lower for the parallel-rib arrangement. This is illustrated by the normalized time- and spanwise-averaged velocity and total pressure data in Fig. 4a and b, and f and g. In contrast, the spanwise-averaged static pressure data in Fig. 4c and h are roughly uniform as Y/H varies, with about the same magnitudes for the parallel- and crossed-rib configurations at $Re_H = 8000$.

Fig. 5 gives four of the same time-averaged quantities which are presented in Fig. 4, except that these data are averaged in the normal direction and shown as they vary

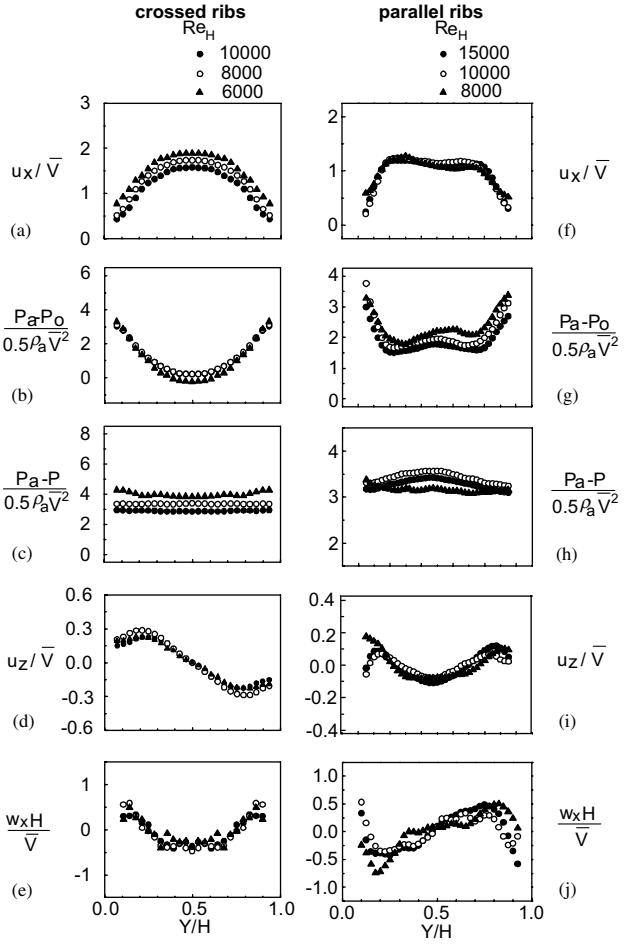

Fig. 6. For crossed-rib turbulators from surveys conducted in a spanwise-normal plane at $X = 1235$ mm for different Reynolds numbers, Re_H, spanwise-averaged and time-averaged profiles of: (a) local streamwise velocity, (b) local total pressure, (c) local static pressure, (d) local spanwise component of velocity, and (e) local streamwise vorticity. For parallel-rib turbulators from surveys conducted in a spanwise-normal plane at $X = 1235$ mm for different Reynolds numbers, Re_H, spanwise-averaged and time-averaged profiles of: (f) normalized local streamwise velocity, (g) normalized local total pressure, (h) normalized local static pressure, (i) normalized local spanwise component of velocity, and (j) normalized local streamwise vorticity.

with Z/H. For the crossed- and parallel-rib turbulators, dimensional magnitudes are presented in Fig. 5a–d, and normalized magnitudes are given in Fig. 5e–h for $Re_H = 8000$. Here, the most important and interesting difference between the crossed- and parallel-rib configurations is the periodicity with Z/H which is produced by the parallel-rib arrangement. Results also show that magnitudes of dimensional streamwise velocity generally decrease with Z/H and that total pressure deficits generally increase with Z/H for the parallel-rib turbulators. Such variations, especially the periodicity, are connected to the flow structures which are produced by the parallel ribs (vortex pairs, individual vortices, and eddy motions shown in Fig. 2b) with length scales which are about equal to the spanwise spacing between adjacent ribs. The periodic variations in Fig. 5 are also due to the effects of individual parallel ribs, as they affect flow which is advected near to and adjacent to them. In particular, the effects of multiple ribs in producing multiple flow perturbations and multiple flow re-circulation zones make contributions to the periodic variations evident in Fig. 5, including the ones evident in the streamwise vorticity. These are especially pronounced in Fig. 5d and h for the parallel ribs.

Fig. 6 shows how spanwise-averaged profiles of normalized streamwise velocity, total pressure, static pressure, spanwise velocity, and streamwise vorticity vary with Reynolds number for the crossed- and parallel-rib turbulator configurations. Each data point in each profile is obtained by averaging survey data in the Z/H direction as Y/H is held constant. Non-dimensional magnitudes of streamwise velocity and static pressure (in

Fig. 6a, c, f, and h) generally decrease for crossed-rib turbulators and increase for parallel-rib turbulators as Reynolds number increases, at each value of Y/H. The location of maximum streamwise velocity magnitudes is in the central part of the channel for both rib arrangements. Non-dimensional magnitudes of spanwise-averaged static pressure are nearly constant over the channel width for the crossed-rib turbulators, but are somewhat higher in the central part of the channel for the parallel-rib turbulators. Non-dimensional magnitudes of total pressure deficit, (in Fig. 6b and g) generally show trends with Reynolds number which are opposite to the variation of streamwise velocity at each Y/H value. Non-dimensional profiles of the spanwise velocity component (in Fig. 6d and i) and streamwise vorticity (in Fig. 6e and j) show only small variations as the Reynolds number changes for both rib configurations.

3.3. Local Nusselt number ratio variations

Baseline Nusselt numbers Nu_0, used to normalize the ribbed channel values, are measured in a smooth rectangular test section with smooth walls replacing the ribbed test surfaces. Except for the absence of the ribs, all geometric characteristics of the channel are the same as when the ribbed test surfaces are installed. These measurements are made in the downstream portion of the test section where the channel flow is hydraulically and thermally fully developed. All Nu_0 baseline values are obtained using a ratio of inlet stagnation temperature to wall temperature of 0.93–0.95. Baseline Nusselt numbers Nu_0 are well represented using an equation given by

$$Nu_0 = 0.023 Re_{D_h}^{0.8} Pr^{0.4} \quad (1)$$

which is valid when uniform heat flux is applied to all four channel surfaces, and the channel flow is hydraulically and thermally fully developed [8,15,16].

The effects of crossed- and parallel-rib turbulators on spatially-resolved Nusselt number ratios are illustrated by the data presented in Fig. 7. These data are obtained with variable surface heat flux and surface conduction analysis applied to the data. In other words, these data account for three-dimensional conduction within the test surface, which is especially pronounced within and near individual-rib turbulators. Nu/Nu_0 data are given as they vary with Z/H for constant $X/H = 11.22$ for Re_H of 17,000 and 18,300. Results show that the highest Nusselt number ratio values are present on the rib tops, especially near the edges, for both rib turbulator configurations. For the data shown in Fig. 7, the rib extends over Z/H from -0.08 to 0.10. $Z/H > 0.10$ are then located upstream of the rib, and $Z/H < -0.08$ locations are then positioned downstream of the rib. The lowered Nu/Nu_0 values over the central part of the rib are due to three-dimensional conduction within the rib, and to convective heat losses from the two vertical sides of the rib [16]. The local Nu/Nu_0 variations shown in Fig. 7 are approximately same for many locations along the test surface for both the crossed- and parallel-rib configurations. This is evident at corner locations, where the ribs join the flat part of the test surface (at Z/H of -0.08 and 0.10), and on the downstream side of the rib. Corner locations correspond to very low Nusselt number ratio magnitudes and significant local hot spots. Downstream of the rib, local Nusselt number ratios increase significantly as Z/H decreases, with relatively low values just adjacent to the rib at $Z/H = -0.08$, for both rib configurations. The most important differences in the local Nu/Nu_0 values between the parallel and crossed-rib configurations are present upstream of the rib at $X/H > 0.10$. Here, the parallel-rib Nusselt number ratios are significantly higher than the crossed-rib ratios. The character of the secondary flows induced by the parallel ribs, especially the secondary flows with length scales which are of the order of the spanwise spacing between adjacent ribs, are partially responsible. These and the other events in the channel give increased secondary advection of heat away from the surface, and increased three-dimensional turbulence transport within the flow for the parallel-rib configuration, relative to the crossed-rib configuration [24].

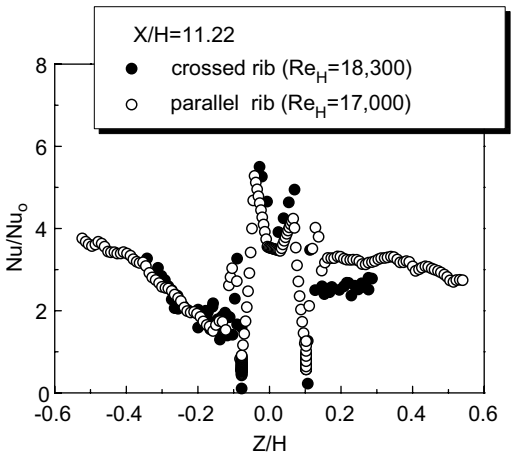

Fig. 7. Local Nusselt number ratios at $X/H = 11.22$ for fully-developed flow conditions for Reynolds numbers Re_H of 17,000 and 18,300, and T_{0i}/T_w of 0.94.

4. Summary and conclusions

Flow structure and surface Nusselt number data are presented for stationary channels with aspect ratio of 4 and angled-rib turbulators inclined at 45° with respect to the streamwise flow direction. Two different rib config-

urations are investigated, one with the ribs parallel and aligned with each other on the two widest channel surfaces, and one with the ribs oriented so that they are perpendicular to each other on the two widest channel surfaces. Results are given at different Reynolds numbers based on channel height from 480 to 18,300, and a ratio of air inlet stagnation temperature to surface temperature of about 0.95. The ratio of rib height to hydraulic diameter is 0.078, the rib pitch-to-height ratio is 10, and the blockage provided by the ribs is 25 percent of the channel cross-sectional area.

Local Nusselt number ratios (determined accounting for three-dimensional conduction within the test surface) are roughly the same for the crossed- and parallel-rib configurations for all locations along the test surface, except just upstream of the ribs. Here, local parallel-rib Nusselt number ratios are significantly higher than local crossed-rib ratios. This is due to significantly different overall and local secondary flows for the two rib configurations, especially secondary flow events with length scales which are of the order of the spanwise spacing between adjacent ribs. For the parallel-ribbed channel, these result in important periodicity of time-averaged flow characteristics (such as streamwise velocity, total pressure, and streamwise vorticity, as they are averaged in the normal or Y/H direction) with Z/H, which is the normalized distance across the span of the channel. Secondary flows (with rib pitch sized length scales) are induced and influenced by the overall secondary flow structure which is present in the ribbed channels. When viewed in flow cross-sectional planes, this consists of one single, large cell of fluid motion for channel with the crossed ribs, whereas two cells of large-scale motion (one in the top half of the channel and one in the bottom half of the channel) are present with the parallel-rib arrangement. These result in regions with high spanwise velocity component gradients near each channel wall with parallel ribs, and one region with high spanwise velocity component gradients in the central part of the channel when crossed-ribs are employed. In addition, time-averaged spanwise-velocity components move in the $+Z/H$ direction near both walls and in the opposite direction in the central part of the channel with parallel ribs, with significantly different motion with crossed ribs. In this case, spanwise velocity is in the positive Z/H direction near the bottom channel wall, and in the negative Z/H direction near the top channel wall. As a result, losses of total pressure and deficits of streamwise velocity are larger in the central part of the channel with parallel ribs mostly because the two large-scale flow cells (which exist over the channel cross-section) are more efficient (than the single cell structure produced by the crossed ribs) in advecting fluid with low streamwise momentum and larger total pressure deficits to the central part of the channel.

Acknowledgements

The work presented in this paper was sponsored by a AGTSR Advanced Gas Turbine Research Program research subcontract sponsored by the US Department of Energy, National Energy Technology Laboratory through a cooperative agreement with the South Carolina Institute for Energy Studies at Clemson University.

References

[1] J.C. Han, L.R. Glicksman, W.M. Rohsenow, An investigation of heat transfer and friction for rib-roughened surfaces, Int. J. Heat Mass Transfer 21 (7) (1978) 1143–1156.
[2] J.C. Han, J.S. Park, Developing heat transfer in rectangular channels with rib turbulators, Int. J. Heat Mass Transfer 31 (1) (1988) 183–195.
[3] J.C. Han, Y.M. Zhang, C.P. Lee, Augmented heat transfer in square channels with parallel, crossed, and v-shaped angled ribs, ASME Trans. J. Heat Transfer 113 (3) (1991) 590–596.
[4] J.C. Han, J.J. Huang, C.P. Lee, Augmented heat transfer in square channels with wedge-shaped and delta-shaped turbulence promoters, Enhanced Heat Transfer 1 (1) (1993) 37–52.
[5] M.E. Taslim, T. Li, D.M. Kercher, Experimental heat transfer and friction in channels roughened with angled, v-shaped, and discrete ribs on two opposite walls, ASME Trans. J. Turbomach. 118 (1) (1996) 20–28.
[6] M.E. Taslim, T. Li, S.D. Spring, Measurements of heat transfer coefficients and friction factors in passages rib-roughened on all walls, ASME Trans. J. Turbomach. 120 (3) (1998) 564–570.
[7] L. Casarsa, M. Cakan, T. Arts, Characterization of the velocity and heat transfer fields in an internal cooling channel with high blockage ratio, in: ASME 47th International Gas Turbine and Aeroengine Congress and Exposition, Amsterdam, The Netherlands, ASME Paper No. GT-2002-30207, 2002.
[8] P.M. Ligrani, G.I. Mahmood, Spatially-resolved heat transfer and friction factors in a rectangular channel with 45-deg angled crossed-rib turbulators, ASME Trans. J. Turbomach. 125 (3) (2003) 575–584.
[9] Z. Wang, P.T. Ireland, S.T. Kohler, J.W. Chew, Heat transfer measurements to a gas turbine cooling passage with inclined ribs, ASME Trans. J. Turbomach. 120 (1) (1998) 63–69.
[10] D. Thurman, D., P. Poinsatte, Experimental heat transfer and bulk air temperature measurements for a multipass internal cooling model with ribs and bleed, in: ASME 45th International Gas Turbine and Aeroengine Congress and Exposition, Munich, Germany, ASME Paper No. 2000-GT-233, 2000.
[11] H.H. Cho, S.Y. Lee, S.J. Wu, The combined effects of rib arrangements and discrete ribs on local heat/mass transfer in a square duct, in: ASME 46th International Gas Turbine and Aeroengine Congress and Exposition, New Orleans, LA, ASME Paper No. 2001-GT-175, 2001.
[12] B. Bonhoff, S. Parneix, J. Leusch, B.V. Johnson, J. Schabacker, A. Bolcs, Experimental and numerical study

of developed flow and heat transfer in coolant channels with 45° ribs, Int. J. Heat Fluid Flow 20 (1999) 311–319.

[13] J. Schabacker, A. Bolcs, B.V. Johnson, PIV investigation of the flow characteristics in an internal coolant passage with 45° rib arrangement, in: ASME 44th International Gas Turbine and Aeroengine Congress and Exposition, Indianapolis, IN, ASME Paper No. 99-GT-120, 1999.

[14] S. Acharya, V. Eliades, D.E. Nikitopoulos, Heat transfer enhancements in rotating two-pass coolant channels with profiled ribs, in: ASME 45th International Gas Turbine and Aeroengine Congress and Exposition, Munich, Germany, ASME Paper No. 2000-GT-227, 2000.

[15] G.I. Mahmood, M.L. Hill, D.L. Nelson, P.M. Ligrani, H.-K. Moon, B. Glezer, Local heat transfer and flow structure on and above a dimpled surface in a channel, ASME Trans. J. Turbomach. 123 (1) (2001) 115–123.

[16] G.I. Mahmood, P.M. Ligrani, K. Chen, Variable property and temperature ratio effects on Nusselt numbers in a rectangular channel with 45 deg angled rib turbulators, ASME Trans. J. Heat Transfer 125 (5) (2003) 769–778.

[17] P.M. Ligrani, B.A. Singer, L.R. Baun, Miniature five-hole pressure probe for measurement of three mean velocity components in low speed flow, J. Phys. E—Sci. Instrum. 22 (10) (1989) 868–876.

[18] P.M. Ligrani, B.A. Singer, L.R. Baun, Spatial resolution and downwash velocity corrections for multiple-hole pressure probes in complex flows, Exp. Fluids 7 (6) (1989) 424–426.

[19] P.M. Ligrani, Flow visualization and flow tracking as applied to turbine components in gas turbine engines, Measure. Sci. Technol. 11 (7) (2000) 992–1006.

[20] F. Kreith, M.S. Bohn, Principles of Heat Transfer, fourth ed., Harper & Row, New York, 1986.

[21] S.R. Sargent, C.R. Hedlund, P.M. Ligrani, An infrared thermography imaging system for convective heat transfer measurements in complex flows, Measure. Sci. Technol. 9 (12) (1998) 1974–1981.

[22] S.J. Kline, F.A. McClintock, Describing uncertainties in single sample experiments, Mech. Eng. 75 (1953) 3–8.

[23] R.J. Moffat, Describing the uncertainties in experimental results, Exp. Therm. Fluid Sci. 1 (1) (1988) 3–17.

[24] P.M. Ligrani, M.M. Oliveira, T. Blaskovich, Comparison of heat transfer augmentation techniques, AIAA J. 41 (3) (2003) 337–362.